

# COMPARATIVE ASSESSMENT OF MATERIAL PERFORMANCE IN DEMO FUSION REACTORS

M. R. GILBERT,\* S. ZHENG, R. KEMP, L. W. PACKER, S. L. DUDAREV, and J.-CH. SUBLET

CCFE, Culham Science Centre, Abingdon, OX14 3DB, United Kingdom

Received November 11, 2013

Accepted for Publication March 24, 2014

<http://dx.doi.org/10.13182/FST13-751>

*A key goal for fusion materials modelling research is the development of predictive simulation models and capabilities to assess material performance under the neutron irradiation conditions expected in near-plasma regions of fusion reactor tokamaks. This paper presents computational results from the modelling of neutron fields in the latest concepts for the next-step demonstration fusion reactor, DEMO. In particular, the variation in neutron exposure as a function of coolant choice and tritium-breeding blanket concept are described, and the calculated neutron spectra are then applied to predict*

*damage rates, helium production rates, and helium-induced grain-boundary embrittlement lifetimes—updating previous estimates derived using an earlier DEMO model.*

**KEYWORDS:** computational assessment of material performance, helium embrittlement of grain boundaries, DEMO fusion reactor

*Note: Some figures in this paper may be in color only in the electronic version.*

## I. INTRODUCTION

The successful realisation of fusion energy for power production depends heavily on the development of materials able to withstand the extreme conditions expected in near-plasma regions of reactors. In particular, the neutron irradiation experienced within the vacuum vessel (VV) of a fusion reactor will cause degradation of material performance, including loss of strength, increased brittleness, radiation-induced swelling, and reduction in structural integrity. However, to make a reactor both physically and commercially viable, components must remain within operational parameters for sufficient time. Reliable estimates of component lifetimes are an important part of power plant design and engineering, since planned maintenance and shutdown time is expensive, and therefore these lifetimes have a direct

impact on the cost of electricity. Hence a primary goal for fusion materials modelling research is the development of predictive simulation capabilities to assess material performance and lifetimes under fusion neutron irradiation. Such predictions will aid the engineering design and material selection studies.

Previously,<sup>1,2</sup> we have described integrated computational studies that take the results of (Monte Carlo) neutron-field mapping simulations on full 3D reactor designs, and, using a combination of neutron-induced transmutation (inventory) calculations and helium-induced grain boundary embrittlement atomistic modelling, provided lifetime-before-failure estimates for a range of materials important for fusion reactor design. Specifically, the estimates were performed for a conceptual design, developed in 2009, of the next-step demonstration reactor (DEMO). In the present work we apply the integrated techniques to updated (2013) DEMO models, which incorporate a range of cooling and tritium-breeding concepts into a fixed reactor geometry.

\*E-mail: mark.gilbert@ccfe.ac.uk

Additionally, the latest computational tools are applied to estimate the variance in the displacements-per-atom (dpa) measure of radiation damage accumulation, with significant variation observed as a function of DEMO concept. We also discuss the need to move beyond the concept of dpa, to more accurate methods of predicting the evolution in radiation damage under a given neutron field.

## II. NEUTRON TRANSPORT SIMULATIONS

The basic DEMO design used in the present study is a 1.8 GW device (2.2 GW total thermal power – including heat multiplication within the lithium breeder blanket). The operation and geometry parameters were created using the PROCESS code<sup>3,4</sup> as part of the European Fusion Development Agreement (EFDA) Power Plant Physics & Technology (PPPT) working group on DEMO. The concept has a plasma major radius of 9 m, with an aspect ratio of 3.616, and an average neutron wall loading of  $1.1 \text{ MW m}^{-2}$  (Ref. 5). The divertor is primarily tungsten (W), with a Eurofer-based first wall (FW) and Inconel-718-based vacuum vessel (VV).

The HERCULES system code<sup>6,7</sup> was used to generate a finite-element (cell-based) geometry of the model as the input to the Monte Carlo neutron transport simulations with MCNP (Ref. 8). HERCULES was used to create four different combined coolant-choice and tritium-breeder concepts for the present geometry, based on the power plant conceptual study (PPCS) (Ref. 9). These are, respectively, a helium-cooled reactor with a tritium-breeding blanket made up of Li + Be pebbles (designated as hcpb here), a helium-cooled reactor with a self-cooling liquid LiPb blanket (hcll), a water-cooled reactor with the liquid blanket (wcll), and, while not strictly part of the original PPCS, but added to the set for comparison, a water-cooled Li + Be ceramic breeder concept (wcbb).

The aim in the present study was to keep the variation between the different models as small as possible and so the geometries of each concept are identical. In particular, the geometry of the template radial build used for the models, created using PROCESS, was based on the PPCS-A/B concept,<sup>9</sup> which is equivalent to the hcpb concept included in the present study. The only concept-specific modifications made to produce the different models was alteration of the appropriate materials and associated densities. Specifically, the coolant was changed in all cells (as necessary) – under the assumption that only one cooling system is realistic in a power plant – and the blanket cells were additionally modified for the particular tritium-breeding concept. Furthermore, to achieve the required tritium-breeding ratio (TBR) for each model, some of the blanket compositions needed significant  $^6\text{Li}$  enrichment to maintain  $\text{TBR} > 1$  (none for hcpb, but 90%  $^6\text{Li}$  enrichment in the two liquid LiPb concepts and 60%  $^6\text{Li}$  enrichment for wcbb).

Using a fixed geometry means that, strictly speaking, the shield thicknesses of approximately 30 cm on the inboard and 80 cm on the outboard side, which are consistent with those reported in Refs. 10 and 11, are only optimised for the hcpb model, although the results presented later demonstrate that they are more than sufficient for both of the water-cooled models. Fully-realistic reactor designs based on the four different coolant and breeding combinations would have very different shielding requirements to protect the VV. However, the results presented here provide a comparison of the different levels of attenuation achieved through the near-plasma components (FW, blanket, and divertor), allowing assessment of the relative shielding efficiency of these structures, and thus how much additional shielding might be required to protect the VV.

Figure 1 shows a 2D poloidal cross section through the geometry created by HERCULES, as well as the spatial and energetic probability distribution of 14 MeV source neutrons used by MCNP. The energies of the neutrons are sampled from a distribution peaked at 14 MeV with a width reflecting the Doppler broadening associated with the 12.87 keV plasma temperature. The spatial probability distribution function was defined using a user-specified subroutine within MCNP that applies the usual equations for the plasma neutron source model described by Wu *et al.*<sup>12</sup>

Each of the four models were run for several weeks with MCNP, in parallel, with 8 compute-cores for each model, producing between 3 and  $15 \times 10^9$  neutron histories. Note that the amount of neutron moderation and multiplication varies with model, making individual histories more, or less, computationally expensive and leading to a different overall number of histories for the same computing time. High resolution energy spectra, containing 616 energy bins (see Ref. 13 for full details of this energy spectrum), were tallied in each finite-element cell of the geometry. It is necessary to use such high resolution energy bins in order to capture the full complexity of the flux spectrum, especially when considering materials with large resonances in their nuclear reaction cross sections (for example, in W, as discussed in Ref. 14). The large number of neutron histories simulated in MCNP allowed the statistics for this high resolution spectrum to be reasonable in the majority of in-vessel regions – with errors typically less than 5% in all energy bins greater than 1 eV for the near-plasma regions. In the deeper penetration regions (e.g. in the VV) the errors are less than 5% down to 0.01 eV, although this is at the expense of the higher energy bins (errors in the low flux MeV bins, see Fig. 2, of some VV regions were around 15%).

Summing the neutron fluxes for a given energy spectrum gives the total flux in  $\text{n cm}^{-2} \text{s}^{-1}$ , which is one measure of the total rate of exposure to neutrons. Note that the total neutron fluence is also proportional to this total flux via integration in time. The total flux in the FW armour regions shows significant variation with model

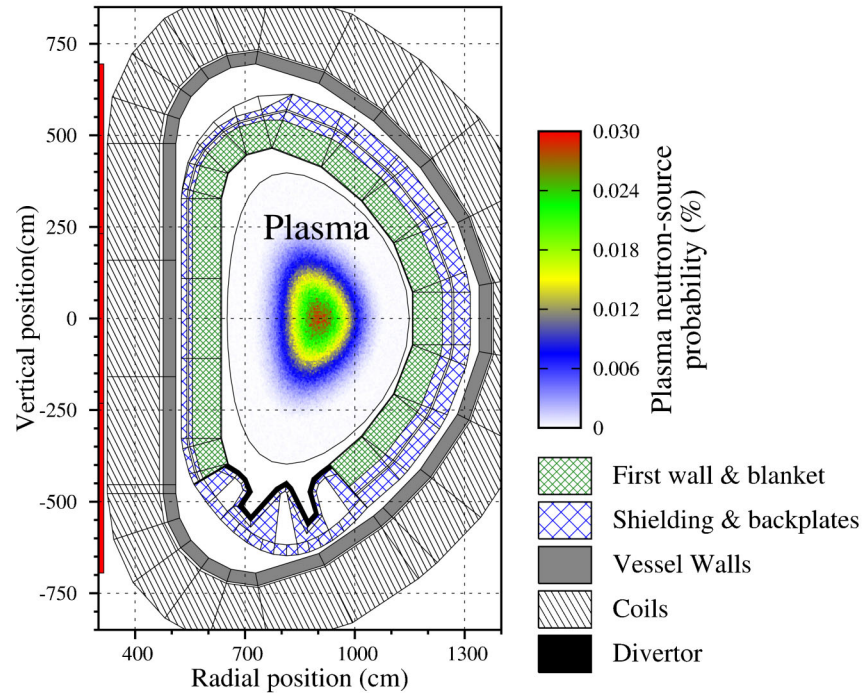


Fig. 1. A 2D poloidal slice through the cell-based geometry created by the HERCULES (Refs. 6 and 7) code and used as input for the neutron transport simulations. Superimposed over the model is a location probability distribution for the plasma neutron source, showing that the peak of the distribution is centred at 9 m (the major radius of the model).

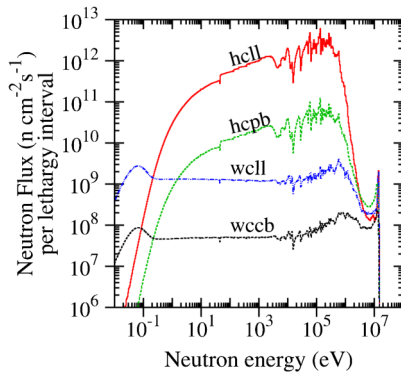


Fig. 2. Comparison of the neutron energy spectra in the equatorial inboard VV wall (position “11” in the schematic shown in Fig. 5) of the four different concepts.

(factor of  $\sim 4$  between the highest and lowest), but also as a function of poloidal angle within a given model. Figure 3 shows that the highest total fluxes are predicted for the helium-cooled LiPb (hcll) concept, with the wcll concept a little lower. The Be+Li ceramic breeder concepts produce lower total fluxes due to a reduced amount of back-scattering from the breeder blanket, compared to the LiPb breeder, with water-cooling also reducing back-scatter. In all models, the highest fluxes are predicted for the equatorial FW armour regions, with the outboard slightly higher than the inboard.

However, the variation in total flux hides some of the important detail associated with the full neutron flux vs. energy spectra. For example, Fig. 4, shows the four neutron energy spectra calculated for the outboard equatorial FW armour position (position “A” in the schematic shown in Fig. 3), which is where the total flux is highest. From the figure it is clear that the four models produce very different spectrum profiles. The ceramic breeder concepts produce highly moderated spectra, even in this near plasma region. Even though the hcll concept has the highest total flux, its spectrum is only high above 10 keV, and is several orders of magnitude lower than the equivalent hcpb concept at lower neutron energies. This, in particular, explains why  $^6\text{Li}$  enrichment was required for all but the hcpb concept – to counter-balance the reduced flux of well-moderated neutrons, which produce the highest tritium production rates, it was necessary to increase the proportion of  $^6\text{Li}$  to maintain breeding efficiency.

In deeper regions of the model geometry the relative comparison between the four concepts changes. For example, for the poloidal variation in total flux that reached the walls of the VV through the fixed thicknesses of blanket and shielding (see Fig. 1) there are orders of magnitude difference between the four concepts (Fig. 5). The hcll model still has the highest fluxes, but hcpb is now second, with total fluxes in the VV wall behind the tritium-breeding blanket (positions 1–13 and 21–26 in

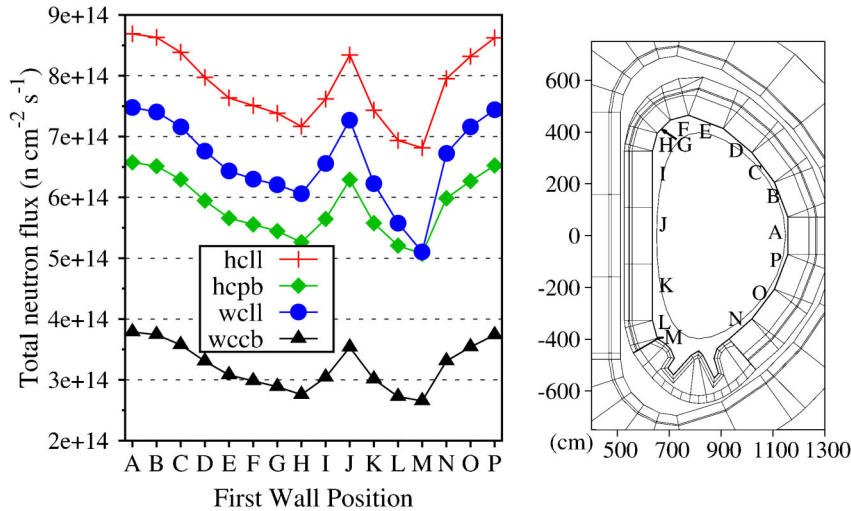


Fig. 3. Poloidal variation in the total flux predicted for the FW armour of the four different concepts. The FW positions of each cell given in the plot (left) are shown in the schematic of the model (right).

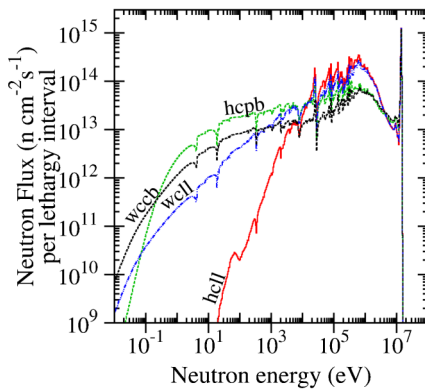


Fig. 4. Comparison of the neutron energy spectra in the equatorial outboard FW armour position (position “A” in the schematic shown in Fig. 3) of the four different concepts.

Fig. 5) around 1.5 orders of magnitude lower. Meanwhile, behind the divertor the only variation with model is due to cooling concept and so both hcll and hcpb, as well as wccl and wccb, show similar levels of attenuation in the corresponding VV positions (positions 14–20 in the figure). However, the fact that, particularly for the hcpb model for which the model geometry is most optimised, the total neutron flux generally increases behind the divertor could indicate a deficiency in the shielding in the present DEMO concept.

Across the entire poloidal extent the total VV fluxes in the wccl model are at least an order of magnitude lower than either of the helium-cooled models, with the wccb model total fluxes lower still. The combined shielding effect of both water cooling and a ceramic breeding

blanket in wccb leads to the predicted total fluxes for the VV wall having a range of between  $1.7 \times 10^6$  and  $1.6 \times 10^{10} \text{ n cm}^{-2} \text{ s}^{-1}$  compared to a range of  $2.0 \times 10^{12}$  to  $1.4 \times 10^{13} \text{ n cm}^{-2} \text{ s}^{-1}$  in the hcll model. While these differences in flux are probably not fully representative of those that would occur in properly optimised models for each concept, they demonstrate that such optimisation would necessarily lead to improved shielding configurations for the helium-cooled concepts, either via increased component thickness or selection of appropriate highly moderating materials.

Similarly to the case for the FW armour, the profile of the neutron spectra calculated for the VV in the four concepts is also very different. Figure 2 shows the inboard equatorial neutron spectra (position “11” in the Fig. 5 schematic) of the VV wall for the four different concepts. The two water-cooled concepts have heavily moderated spectra in this region, with an almost flat profile over much of the energy range. The spectral profile even contains the thermal Maxwellian below 0.1 eV, which is normally difficult to observe in the homogenized materials used for these kinds of neutron-transport simulations, demonstrating that very significant moderation has taken place with the shielding configuration used in the models.

### III. INTEGRATED ASSESSMENT OF HELIUM-INDUCED GRAIN-BOUNDARY TIME TO FAILURE

Previously,<sup>1</sup> a simple model to estimate the maximum concentrations of helium (He) that can be accommodated in grain boundaries (GBs) was applied to estimate the critical time to failure  $t_{\text{He}}^c$  of various pure metallic

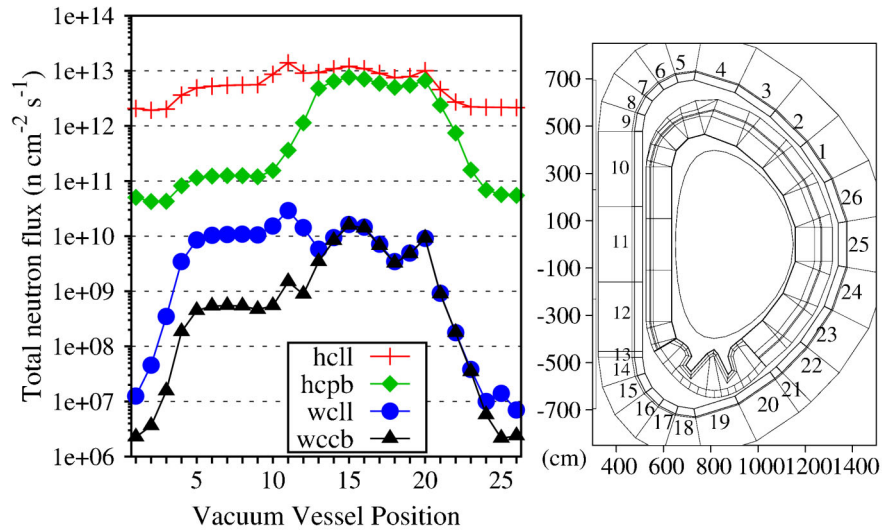


Fig. 5. Poloidal variation in the total flux predicted for the vacuum vessel (VV) wall of the four different concepts. The numbering of each VV cell given in the plot (left) refers to the numbers in the schematic of the model (right).

materials. In particular, experimentally measured surface energies were equated with He solution energies from *ab initio* calculations to define the maximum (or critical) GB concentrations and then, subsequently, nuclear inventory calculations were performed to define bulk helium production rates. These rates were then used to predict the time required to reach the critical concentrations, under the assumption that all bulk He will be transported to the boundary, which is most valid for small grains.

In Ref. 2, this model was refined by suggesting that pre-existing vacancy-like regions would allow the GBs to accommodate more He than originally<sup>1</sup> predicted. The critical GB and bulk He concentrations,  $v_{\text{He}}^c$  and  $G_{\text{He}}^c$ , respectively, given in Ref. 2 and shown in Table I, are used here to give critical time-to-failure values for the outboard equatorial FW armour position for various fusion-relevant materials in each of the four “DEMO2013” concepts discussed earlier (see Table I).

The inventory calculations – to track the time evolution of material composition under a given neutron field – were performed using the EASY-II system (European Activation SYstem), which consists of the FISPACT-II (Ref. 13) inventory code and a large library of nuclear data, including reaction cross sections and decay data. Specifically, data from TENDL 2011 (TALYS-based Evaluated Nuclear Data Library) (Ref. 15) were used, although various others are available as part of EASY-II. As well as tracing the evolution of the heavy element concentrations, FISPACT-II also traces the accumulation of the gas particles emitted from certain nuclear reactions, such as  $(n, \alpha)$  – neutron capture followed by  $\alpha$ -particle ( $^4\text{He}$ ) emission; or  $(n, p)$  – neutron capture followed by proton ( $^1\text{H}$ ) emission. For example, the time evolution over 50 full power years (fpy), which is

a reasonable, if optimistic, reactor lifetime (and the FW certainly wouldn’t last this long), in He concentration for different materials under the outboard equatorial FW armour flux of the hcpb model is given in Fig. 6, showing that, in this scenario, Fe is the worst performer, producing, on average, 100 atomic parts per million (appm) He per fpy, while Ta produces He at the slowest average rate of only 4.5 appm per fpy.

Table I gives the results of the integrated assessment of material lifetimes under He-induced GB embrittlement for the four models under the neutron field for the outboard equatorial FW armour (Fig. 4). Of the seven materials considered, only Fe and Cr have critical times below 10 fpy, and so it is unlikely that this failure mechanism will be a cause for concern for the others (W, Ta, Nb, Mo, or V). It is interesting to note that for certain materials, including Fe, the shortest  $t_{\text{He}}^c$  values are predicted for the hcpb concept, even though the overall flux is lower than in the hcll or wcll models, while in other materials, such as Nb, the hcll has the lowest  $t_{\text{He}}^c$  values – in agreement with the total flux measure. These differences are due to the variation in spectrum profile shown in Fig. 4 combined with the fact that some materials have helium production routes that involve threshold reactions (e.g. Nb), while others (e.g. Fe) do not. In the well-moderated spectra of the ceramic breeder concepts, the reaction probability is high for non-threshold reactions, while for the relatively poorly moderated hcll concept the high fluxes at high neutron energies favour reactions with thresholds.

The table also gives updated estimates, again using the TENDL 2011 nuclear data library, for the original hcpb “DEMO 2009” model.<sup>1</sup> This concept has a higher power output (2.7 GW in 2009 versus 1.8 GW here), and so the  $t_{\text{He}}^c$



TABLE I

Critical Boundary Densities  $\nu_{\text{He}}^c$ , Critical Bulk Concentrations  $G_{\text{He}}^c$ , and Approximate Critical Lifetimes  $t_{\text{He}}^c$  (in DEMO First-Wall Full-Power Time) for He in Various Elements for Both the “DEMO2009” model<sup>1</sup> and the four “DEMO2013” Concepts Presented Here\*

Element	$\nu_{\text{He}}^c$ ( $\text{cm}^{-2}$ )	$G_{\text{He}}^c$ (appm)	$t_{\text{He}}^c$ (fpy) estimates				
			“DEMO2009” <sup>1</sup> (hcpb)	Present study “DEMO2013”			
				hcll	hcpb	wcll	wccb
Fe	$1.08 \times 10^{15}$	764.6	5 (6)	9	6	8	7
Cr	$1.07 \times 10^{15}$	771.9	6 (8)	7	7	7	7
Mo	$1.96 \times 10^{15}$	1833.8	49 (46)	50+	50+	50+	50+
W	$2.71 \times 10^{15}$	2582.1	50+ (50+)	50+	50+	50+	50+
V	$1.41 \times 10^{15}$	1172.2	20 (37)	25	25	25	25
Nb	$2.11 \times 10^{15}$	2275.2	38 (49)	45	47	46	46
Ta	$2.22 \times 10^{15}$	2399.4	50+ (50+)	50+	50+	50+	50+

\*Critical boundary densities and critical bulk concentrations are both from Ref. 2. He production rates were calculated using the latest TENDL 2011 (Ref. 15) nuclear data libraries for the irradiation field predicted for the FW outboard equatorial armour (Fig. 4).  $t_{\text{He}}^c$  estimates from Ref. 2, using nuclear data from the 2003 edition of the European Activation File (EAF) (Ref. 16), are given in brackets for the “DEMO2009” model for comparison. A  $t_{\text{He}}^c$  of “50+” indicates that the He production rates in the material are too low to reach  $G_{\text{He}}^c$  on an optimistic 50-year reactor lifetime. Assumed grain size of 0.5  $\mu\text{m}$ .

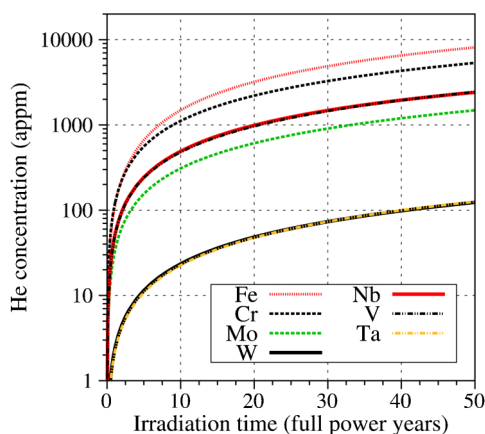


Fig. 6. He production rates calculated for various pure elements under the neutron irradiation field calculated for the outboard equatorial FW armour (position “A” in Fig. 3) of the hcpb model.

estimates are lower for the equivalent FW armour region of the older model – illustrating the uncertainty (in predictions) caused by a frequently changing conceptual design. Note, however, that these predictions with TENDL 2011 are somewhat different from the original predictions<sup>2</sup> (also shown in the table in brackets), which were calculated using a different, older, and less complete, nuclear data library.<sup>16</sup> Such variation highlights the fact that there is still uncertainty and debate surrounding the compilation of such data libraries. Even when libraries have been validated

against measurable experimental values – for example in Refs. 17 and 18, respectively, where decay-heat validations of the TENDL 2011 and EAF2003 (Ref. 16) libraries used here have been performed – subtle differences can produce significant variation in derived quantities such as helium production rates. Uncertainty estimates for the nuclide composition, based on the reaction cross section uncertainties available in the latest data libraries, are part of the ongoing development of the FISPACT-II (Ref. 13) inventory code, and so  $t_{\text{He}}^c$  uncertainties will be available in the future.

#### IV. RADIATION DAMAGE

In addition to the changes in material behaviour caused by transmutation, as considered in the integrated assessment discussed above, neutron irradiation in the fusion environment will also lead to the accumulation of damage resulting from the recoil cascades initiated by the interaction of the neutrons with the constituent atoms (or molecules) of materials. One measure of this “structural” damage is the so-called displacements per atom (dpa) estimate.

The latest nuclear data libraries available through the EASY-II system include displacement damage cross sections generated and processed from the original point-wise nuclear reaction cross sections by the NJOY nuclear data processing system developed at Los Alamos National Laboratory in the United States.<sup>19</sup> Within a given inventory calculation, FISPACT-II (Ref. 13) uses these to calculate the standard Norgett-Robinson-Torrens (NRT) (Ref. 20) dpa for the entire nuclide inventory. This is a

significant advancement on the previous capabilities, where only the dpa in pure elements were considered, as it allows for the estimation of dpa/fpy for complex alloys, and also enables the dpa-rate to be traced as a function of time as the composition changes – if the transmutation rates of a particular material are sufficiently high the dpa/fpy could change significantly. However, dpa rates calculated for alloys in this way can only ever be a (further) approximation, on top of those inherent to the NRT dpa concept itself (see the next section). They do not take into account, for example, the fact that some of the constituent nuclides may only be present as part of molecules, such as oxides in steels, and would thus have very different displacement characteristics, including displacement threshold energies, to what they would have as isolated free nuclides.

Figure 7, shows the poloidal variation in FW armour dpa/fpy in the Eurofer alloy that is the primary constituent of the FW armour tiles in the DEMO models (90% by volume). Results were obtained for each of the four DEMO concepts by taking the average damage rate during a 1 fpy irradiation. Note that in Eurofer, and the other materials considered here, the transmutation rates are not sufficient to produce much variation in the dpa/fpy values, even over a longer, 5 fpy irradiation. All of the dpa/fpy values were obtained using the same TENDL 2011 nuclear data library used for the He production rate calculations discussed in the previous section. As with the total flux (Fig. 3), the hcll concept produces the greatest estimated damage rates (dpa/fpy maximum of  $\sim 20$ ), followed by the equivalent water-cooled concept wcll ( $\sim 18$  dpa/fpy max.), and then the two ceramic breeder

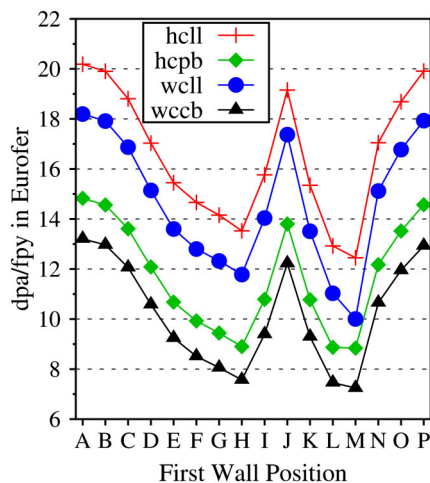


Fig. 7. FW armour poloidal variation in dpa/fpy in Eurofer (9.5 wt.% Cr, 1.2% W, 0.6% Mn, 0.25% V, 0.12% C, 0.09% Ta, 0.045% N, 0.01% O, and Fe the remainder) for each of the DEMO concepts. The FW position given along the x-axis corresponds to the labels in the schematic in Fig. 3.

models (maximum dpa/fpy of  $\sim 15$  and  $\sim 13$ , respectively, for hcpb and wccb). The relative variation is also similar to that observed with the total flux.

Equivalently, Figs. 8 and 9 show the dpa/fpy variation with position for the main material of, respectively, the VV wall, which contains between 60 and 80% Inconel-718 by volume (depending on cooling concept), and the 100% tungsten divertor armour. In Fig. 8, the Inconel-718 dpa/fpy values are tiny compared to the Eurofer values for the FW because the level of neutron-attenuation is significant, but, despite this, the end of lifetime dpa levels for the VV wall, which must last for as long as the reactor is operational, are of the order of several dpa in this DEMO model for the He-cooled concepts (e.g. 0.1 dpa/fpy would produce 3 total dpa after a typical 30-year reactor operation), and orders of magnitude lower for the water-cooled equivalents. This again suggests a potential benefit of choosing water-cooling – the shielding requirements to protect the VV and beyond could be lower, with resulting improvements in the economical viability of the reactor.

The peak dpa/fpy values for W in the divertor armour are roughly half of those calculated for Eurofer in the FW armour, while the minimum damage rates, observed in the high heat-flux regions, which are nonetheless comparatively well shielded from neutrons, are only 1 or 2 dpa/fpy across all four DEMO concepts.

#### IV.A. Beyond dpa

Before summarising the data presented in this paper, it is worth noting the limitations associated with the dpa/fpy measure discussed above. While the integrated assessment of He-induced GB embrittlement provides a complete

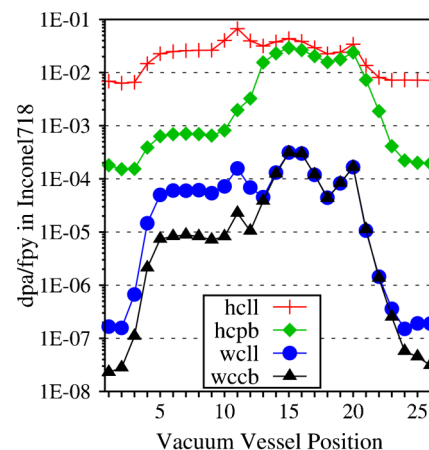


Fig. 8. VV poloidal variation in dpa/fpy in Inconel-718 (55.0 wt.% Ni, 18.0% Fe, 19.0% Cr, 3.0% Mo, 5.0% Nb) for each of the DEMO concepts. The numbering along the x-axis corresponds to the positions identified in the schematic in Fig. 5.

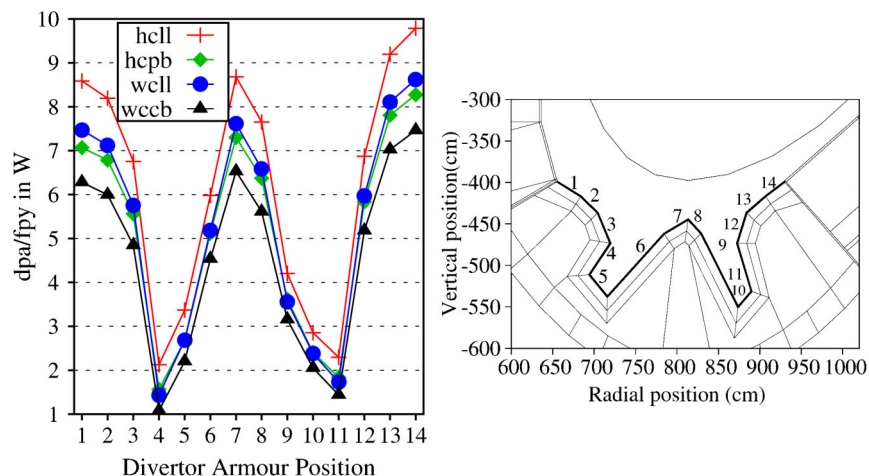


Fig. 9. Divertor armour variation in dpa/fpy in pure W for each of the DEMO concepts. The position numbering along the x-axis of the plot (left) corresponds to the labels in the schematic on the right, which is a close-up of the divertor.

picture, from neutron-transport simulations of an engineered reactor design, through calculations of neutron-induced changes in composition, to engineering relevant predictions of material lifetime, using those same neutron-transport simulations to predict dpa rates does not. The NRT dpa measure does not say anything about defect evolution – it merely estimates the number of Frenkel pairs created in a given recoil cascade, with a multiplication factor to estimate recombination effects. In this sense dpa is just an “atom-based” measure of neutron exposure. We have also noted previously<sup>2</sup> that dpa estimates are subject to significant variation with nuclear data, making it difficult to draw any confident conclusions about their meaning.

A fully integrated assessment of radiation damage must include simulation and modelling of the evolution of defects, both within the initial cascade event, and subsequently, at longer times, as the defects from different events interact. A more useful link from neutron transport results to materials modelling is a full description of the initial recoil events for a given neutron irradiation field because this could be combined with energy dependent statistics of cascades to build up a picture of the total damage accumulation. Research findings in this area will be presented in future publications.

## V. SUMMARY

In this paper we have presented the results of integrated assessment studies for the latest conceptual designs for the next-step demonstration fusion power plant. Four different combined cooling and tritium-breeding blanket concepts were considered: a He-cooled reactor with a Be + Li ceramic pebble-bed blanket(hcpb); a He-cooled reactor with a liquid LiPb blanket (hcll); a water-cooled reactor with a LiPb

blanket (well); and a water-cooled device with a Be + Li ceramic breeder (wccb).

Neutron transport simulations, performed using the Monte Carlo code MCNP (Ref. 8), revealed that there is significant variation in both the total flux and flux vs. energy profile as a function of the four different DEMO concepts. Specifically, in near-plasma regions, neutron moderation, which is required for efficient tritium-breeding, is greater with the Be + Li ceramic concepts, while in deeper regions water cooling improves overall levels of attenuation, potentially reducing the amount of shielding required to protect the vacuum-vessel and beyond.

Time-to-failure estimates for He-induced grain-boundary embrittlement, predicted using He production rates obtained from inventory calculations under the simulated neutron irradiation fields, indicate that, even in the FW armour, only certain metallic materials (Fe + Cr) produce He at the required rate to make such a failure mechanism a likely cause for concern.

The latest computational tools and nuclear data evaluations were utilised to provide estimates of the radiation damage rates, measured as dpa/fpy, for complex alloys such as Eurofer and Inconel-718. The dpa/fpy values predicted for Inconel-718 in the VV walls of the DEMO model used here indicated that the end-of-life dpa levels with the He-cooled concepts are non-negligible, but negligible with water-cooling in the fixed geometry of the present DEMO model, suggesting that the optimised shielding requirements would be much reduced in a water-cooled reactor.

## ACKNOWLEDGMENTS

This work was funded by the RCUK Energy Programme [grant number EP/I501045] and by the European Union's



Horizon 2020 research and innovation programme. To obtain further information on the data and models underlying this paper please contact [PublicationsManager@ccfe.ac.uk](mailto:PublicationsManager@ccfe.ac.uk). The views and opinions expressed herein do not necessarily reflect those of the European Commission.

## REFERENCES

1. M. R. GILBERT et al., "An Integrated Model for Materials in a Fusion Power Plant: Transmutation, Gas Production, and Helium Embrittlement Under Neutron Irradiation," *Nucl. Fusion*, **52**, 083019 (2012); <http://dx.doi.org/10.1088/0029-5515/52/8/083019>.
2. M. R. GILBERT et al., "Neutron-Induced dpa, Transmutations, Gas Production, and Helium Embrittlement of Fusion Materials," *J. Nucl. Mater.*, **442**, S755 (2013); <http://dx.doi.org/10.1016/j.jnucmat.2013.03.085>.
3. P. J. KNIGHT, *A User's Guide to the PROCESS Systems Code*, Version 2.1.0, UKAEA Fusion (1996).
4. T. C. HENDER et al., "Physics Assessment for the European Reactor Study," AEA FUS 172, UKAEA/Euratom Fusion Association (1992).
5. R. KEMP, "DEMO1 Parameters, EFDA," EFDA\_D\_2LK7PH (Apr. 2013).
6. P. J. KARDITSAS, "Lifetime Performance Analysis of HCPB Power Plant In-Vessel Components Using HERCULES," *Fusion Eng. Des.*, **83**, 1638 (2008); <http://dx.doi.org/10.1016/j.fusengdes.2008.07.016>.
7. R. PAMPIN and P. J. KARDITSAS, "Fusion Power Plant Performance Analysis Using the HERCULES Code," *Fusion Eng. Des.*, **81**, 1231 (2006); <http://dx.doi.org/10.1016/j.fusengdes.2005.09.054>.
8. J. GOORLEY et al., "MCNP Home Page": <http://mcnp.lanl.gov/> (current as of Nov. 11, 2013).
9. D. MAISONNIER et al., "Power Plant Conceptual Studies in Europe," *Nucl. Fusion*, **47**, 1524 (2007); <http://dx.doi.org/10.1088/0029-5515/47/11/014>.
10. U. FISCHER et al., "Model Generation and Neutronic Design Analyses for the European DEMO Conceptual Study," final report on EFDA task TW6-TRP-005, Deliverable 1a, Forschungszentrum Karlsruhe (July 2008).
11. U. FISCHER et al., "Neutronics Design Analyses of Fusion Power Reactors Based On a Novel Integral Approach," *Fusion Eng. Des.*, **84**, 323 (2009); <http://dx.doi.org/10.1016/j.fusengdes.2008.12.062>.
12. Y. WU et al., "Analysis on Nuclear Heating in the Superconducting Coils of HT-7U Tokamak Fusion Device," *Fusion Eng. Des.*, **66-68**, 1013 (2003); [http://dx.doi.org/10.1016/S0920-3796\(03\)00247-3](http://dx.doi.org/10.1016/S0920-3796(03)00247-3).
13. J.-CH. SUBLET et al., "The FISPACT-II User Manual," CCFE-R(11)11 Issue 4 (2013); see also <http://www.ccfe.ac.uk/EASY.aspx> (current as of Nov. 11, 2013).
14. M. R. GILBERT and J.-CH. SUBLET, "Neutron-Induced Transmutation Effects in W and W-Alloys in a Fusion Environment," *Nucl. Fusion*, **51**, 043005 (2011); <http://dx.doi.org/10.1088/0029-5515/51/4/043005>.
15. A. J. KONING and D. ROCHMAN, "TENDL-2011" (Dec. 29, 2011); <ftp://ftp.nrg.eu/pub/www/talys/tendl2011/tendl2011.html> (current as of Nov. 11, 2013).
16. R. A. FORREST, "The European Activation File: EAF-2003 overview," UKAEA FUS 484 (2002).
17. J.-CH. SUBLET and M. R. GILBERT, "Decay Heat Validation, FISPACT-II & TENDL-2012, 2011 and EAF-2010 Nuclear Data Libraries," CCFE-R(13)20 (2013); see also <http://www.ccfe.ac.uk/EASY.aspx> (current as of Nov. 11, 2013).
18. J.-CH. SUBLET and F. MAEKAWA, "Decay Power: A Comprehensive Experimental Validation," CEA-R-6213 (2009); <http://www.ccfe.ac.uk/EASY2007.aspx> (current as of Nov. 11, 2013).
19. R. E. MacFARLANE et al., "The NJOY Nuclear Data Processing System, Version 2012," LA-UR-12-27079, Los Alamos National Laboratory; <http://t2.lanl.gov/nis/publications/NJOY2012.pdf> (current as of Nov. 11, 2013).
20. M. J. NORGETT et al., "A Proposed Method of Calculating Displacement Dose Rates," *Nucl. Eng. Des.*, **33**, 50 (1975); [http://dx.doi.org/10.1016/0029-5493\(75\)90035-7](http://dx.doi.org/10.1016/0029-5493(75)90035-7).